

Automated Detection of Hyperbola-Shaped Signature in Subbottom Profiler Sonar Image With Morphological Processing

Pengcheng Chen^{ID}, Graduate Student Member, IEEE, Shaoping Lu^{ID}, and Chen Cai^{ID}

Abstract—Subbottom profilers (SBPs) using shipboard sonar can acquire massive amounts of data during exploration missions. Some geological intrusions and artificially buried objects show hyperbola-shaped signatures in the SBP images. These signatures are valuable information, but their detection is time-consuming. In addition, noise and geometric spread further increase the difficulty of detection. This article proposes an automated detection method of hyperbola-shaped signatures in SBP images by utilizing morphological processing. The proposed method can be summarized into four steps: preprocessing, segmentation, morphological processing, and fitting. The morphological processing is the critical technology in the proposed method, including opening, dilation, and skeletonization. Trend curves of signatures can be outlined without a priori knowledge by exploiting morphological processing. The fitting algorithm can refine the curves further into an analytical curve. We validate the feasibility and effectiveness of the proposed method in field data acquired from the Marianas region. Meanwhile, we demonstrate that the proposed method better detects ill-shaped and large curvature hyperbola-shaped signatures. Compared with the template matching and the column-connection clustering (C3) methods, the proposed method can provide better precision and recall using an optimized threshold. In addition, the proposed method is a general detection methodology that can be applied to any SBP images with proper parameters. In conclusion, the morphological processing presented in this article can be employed as a generic hyperbola-shaped signature detection module in SBP image processing.

Index Terms—Hyperbola-shaped signature, morphological processing, subbottom profiler (SBP).

I. INTRODUCTION

SUBBOTTOM profiler (SBP) is an extensively applied marine geophysical instrument [1], [2], [3]. It is an economical navigational exploration tool that uses shipboard sonar

Manuscript received 18 March 2024; revised 7 July 2024; accepted 11 August 2024. Date of publication 14 August 2024; date of current version 27 August 2024. This work was supported in part by the National Natural Science Foundation of China under Grant 42074123, Grant 42230805, and Grant 42106067; in part by the National Key Research and Development Plan of China under Grant 2023YFF0803301; in part by the Natural Science Foundation of Guangdong Province under Grant 2022A1515010090; in part by Shanghai Sheshan National Geophysical Observatory under Grant SSOP202102; and in part by Guangzhou Science and Technology Planning Project under Grant 202102020456. (*Corresponding author: Chen Cai*)

The authors are with the School of Earth Sciences and Engineering and Guangdong Provincial Key Laboratory of Geodynamics and Geohazards, Sun Yat-sen University, Guangzhou, Guangdong 510275, China, and also with the Southern Marine Science and Engineering Guangdong Laboratory (Zhuhai), Zhuhai, Guangdong 519000, China (e-mail: chenpengcheng66@outlook.com; lushaoping@mail.sysu.edu.cn; caich28@mail.sysu.edu.cn).

Digital Object Identifier 10.1109/TGRS.2024.3443412

to acquire high-resolution (decimeter-level) seismic profiles from shallow subseafloor [4]. Due to the sonar directivity pattern, local perturbations (geological irregularities and obstacles) present particular hyperbola-shaped signatures in SBP images [5]. These signatures contain precious information for geological interpretation. However, in SBP surveys, a massive amount of data can be generated due to the underway acquisition mode, which renders manual detection very time-consuming. Therefore, it is necessary to develop a method to automatically detect the signatures. In field data, the signatures tend to be weak and in some sense indistinct due to the rapid geometric spread and attenuation, which means the detection is complex. Interference from background noise and backscattering further fuzz up the shape of hyperbolas. Furthermore, in some scenarios, such as in the deep sea, ill-shaped signals are generated, which can be asymmetry, parts of the hyperbola branches missing, distortion, etc., and can further increase the difficulty of detection.

In the literature, few works are dedicated to addressing the issue of hyperbola-shaped signature detection in SBP images. Some researchers have used SBP as an auxiliary device [6], [7]. The other device, such as a magnetometer, locates the position of the object, and then, the interpreter checks for the hyperbola-shaped signatures at this position. In some research, the template matching method is applied to detect hyperbolas directly. In [8], a hyperbolic template is synthesized to match predetected edges. In [9], a deep learning method is employed to generate a trained model to extract the regions of interest (ROIs) containing hyperbolas. These methods depend on the quality of the synthesis data. As a result, a priori knowledge is indispensable. In general, the existing algorithms are practical for clear shape signatures of a given target. Till now, relevant works have yet to focus on the detection without a priori knowledge of SBP images acquired from complex environments. With the growth of deep-sea exploration tasks, developing a method for automatic detection of well- or ill-shaped hyperbola-shaped signatures is essential.

Many researchers have devoted to detecting hyperbolas in ground-penetrating radar (GPR) images. The mode of GPR devices is similar to the SBP. Both of them work at normal incidence in a monostatic configuration; hence, it is beneficial to review the studies of GPR. In GPR image processing, a two-step method is a popular framework. The method usually starts with obtaining the ROI or geometry from the original data by using threshold method [10], [11], [12], edge detection [13],

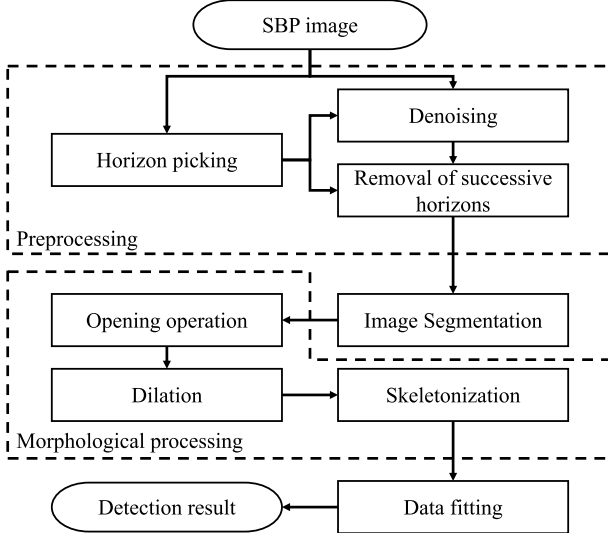


Fig. 1. Block diagram of the proposed method.

[14], time of flight [15], or machine learning method [16], [17]. After that, a hyperbola fitting algorithm is applied. The algorithms include, but are not limited to, Hough transform-based methods [15], [16], [17], Radon transform-based methods [18], the least-squares methods [11], and machine learning-based methods [10], [12].

In this article, we propose an automated detection method of hyperbola-shaped signatures in SBP images with morphological processing. The proposed method can automatically detect well- or ill-shaped hyperbolas without a priori knowledge of SBP image. As shown in the block diagram of the proposed method in Fig. 1, the method can be summarized into four steps: preprocessing, segmentation, morphological processing, and fitting. The steps within the dashed box are suboperations. First and foremost, preprocessing filters out signals that are unrelated to the hyperbola-shaped signatures. Then, a flood-fill-based image segmentation method is applied to distinguish between the signature and the background. The morphological processing further processes the segmented signature into a 1-pixel wide trend curve. Finally, the fitting algorithm is employed to refine the trend curves further into an analytical curve, which is the detection result of the proposed method.

The rest of this article is structured as follows. In Section II, we present some background and issues and elaborate on the proposed hyperbola-shaped signature detection method. Section III provides the experimental results. This article closes with discussion and conclusion in Sections IV and V, respectively.

II. METHOD

A. Problem Description

As a monostatic configuration device, SBP can be regarded as a zero-offset seismic profiler. Consider a single point scatterer in a zero-offset section, as shown in Fig. 2(a). O is the starting point of the voyage and the origin of the coordinates in the SBP image. The minimum travel time (t_{\min}) is

$$t_{\min} = \frac{2h}{v} \quad (1)$$

where h is the depth of the point scatterer, and v is the velocity of the subsurface medium. The two-way travel time of the wave (t) is a function of horizontal distance (x), which is calculated as

$$t = \frac{2\sqrt{(x - x_0)^2 + h^2}}{v} \quad (2)$$

where x_0 is the position of the point scatterer on the x -axis.

By squaring and rearranging, (2) can be rewritten as

$$\frac{t^2}{a^2} - \frac{(x - x_0)^2}{b^2} = 1 \quad (3)$$

where $a = t_{\min}$ and $b = h = v \cdot t_{\min}/2$. In SBP images, v is usually set to 1500 m/s. The travel time curve for the scattered arrival is a hyperbola with the vertex directly at the point scatterer, as shown in Fig. 2(b). The genesis of hyperbolas is known as diffraction in seismology [19]. Theoretically, two hyperbola branches on the coordinate are symmetrical about the center point $(x_0, 0)$. In fact, both x and t in the image are greater than 0, so the hyperbolas are manifested as “south-opening” branches in the SBP images [10].

The travel time dominates the hyperbola shape in SBP images, while its properties, such as amplitude, are affected by other factors. We synthesized a hyperbola-shaped signature using the convolutional model according to Zheng et al. [9]. They have concluded that the signature is impacted by four primary variables, i.e., Earth impulse response, wavelet, propagation loss, and directivity pattern. The Earth impulse response and the wavelet determine the amplitude of the signature. The propagation loss and the directivity pattern are two functions of the energy loss. As depicted in Fig. 2(c), we derived a hyperbola-shaped signature by employing a sinusoidal function as a wavelet, and then, its amplitude is normalized. The energy converges at the vertex of the hyperbola and attenuates gradually along the sides. It is desirable that the signature is clear, smooth, continuous, and effortlessly identifiable. Unfortunately, however, the signature is somewhat indistinct and indecipherable in field data [see Fig. 2(d)].

Fig. 3 shows a typical image that includes a hyperbola-shaped signature, some horizons, and noise. We resize the image for better viewing, and the actual size of the image is 800 × 150 pixels. Besides, to ensure the observability of the weak hyperbola-shaped signature, we increased the contrast of the images. Some of the properties in SBP images also cause detection problems. The impact factors are as follows.

- 1) *Gap Between Lateral and Axial Resolution:* Although SBP images offer an axial resolution on the decimeter scale, the lateral resolution is generally on the meters scale. The gap is even more significant in some long-distance surveys, where the lateral data appear sparser. The primary factor of this problem is the underway mode of acquisition. The gap is visualized on the SBP image, rendering the signature continuity worse. In Fig. 3, the sampling frequency of sonar equipment is approximately 0.2 ms (1/4800 s), so the resolution is 0.3125 m in the axial direction (the resolution in the axial direction is obtained by time-depth conversion using 1500 m/s). The survey vessel collects data at

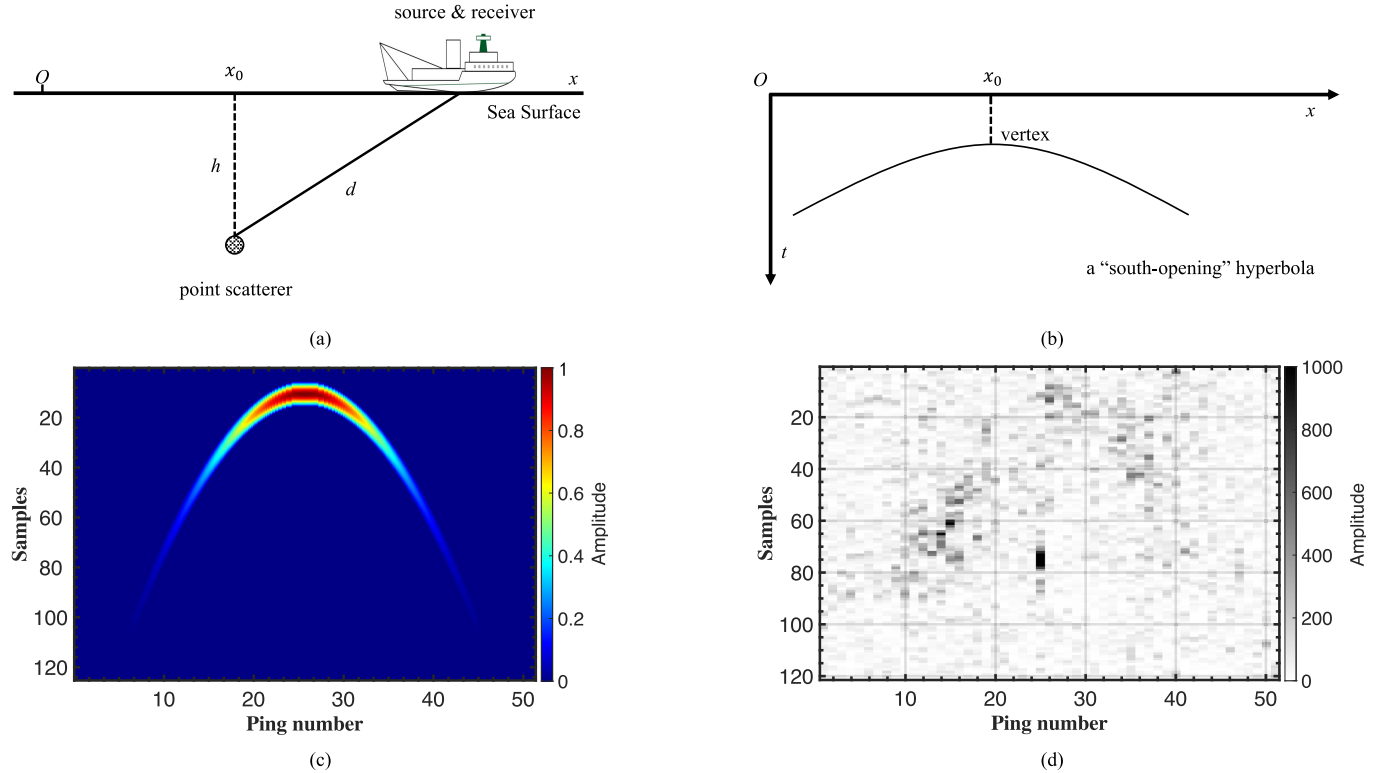


Fig. 2. Seismic diffraction hyperbola principle and signature samples. (a) Single point scatterer in a zero-offset section. (b) “South-opening” hyperbola is produced by the point scatterer in the SBP image. (c) Hyperbola-shaped signature generated according to the theoretical formula. (d) Hyperbola-shaped signature from real data.

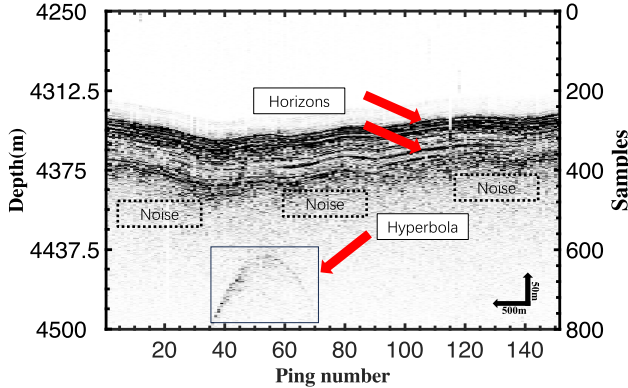


Fig. 3. Example image of field data. The figure shows that the image includes a hyperbola-shaped signature, some horizons, and noise. The left side of the profile is marked with the depth, which was estimated using a constant velocity (1500 m/s). Ping number and samples, respectively, correspond to the pixel index in the picture and have no actual physical meaning.

40-m intervals during the cruise, so the lateral resolution is 40 m. A scale bar is added in the lower right corner of Fig. 3 to manifest the lateral and axial resolutions.

- 2) *High Noise and Backscattering:* Noise refers to external additions disturbing the expected signals, and backscattering is the reflection from the microscale topography of the interface. These noises are labeled in Fig. 3. Noise and backscattering could alias the signatures, obscuring the shape of the hyperbolas.
- 3) *Sharpness of the Wavelet:* The wavelet in the SBP image is processed into an impulse response [20]. A sharp wavelet does avoid signal aliasing, but it weakens the geometry of the shapes. In particular, for the data with

a low signal-to-noise ratio, the problem of weakening becomes more apparent.

- 4) *Overall Weakness:* Hyperbola-shaped signatures are generally at least an order of magnitude smaller than successive horizons due to the rapid geometrical spreading and attenuation.
- 5) *Hyperbolic Misshapeness:* The hyperbola in Fig. 3 is a misshapen signature. The right side of the signature is almost too weak to be identified. The origins of ill-shaped are complex issues. Currently known candidates include, but are not limited to, uneven distribution of sediment acoustic velocity, device attitude changing, mutual wave interactions, the sonar directivity pattern, and the intrinsic shape of the object.

B. Preprocessing

In Section II, we use Fig. 3 as a demo image to demonstrate the results of each step of the proposed method. To demonstrate image processing better, our later images in this section will not show the physical dimensions corresponding to the axes.

Before processing the SBP images, a series of preprocessing techniques is employed on the field data. The purpose of this step is to filter out signals that are not related to the hyperbola-shaped signature, including horizons and noise. A preprocessing procedure is implemented for the following: 1) horizon picking; 2) denoising; and 3) removal of successive horizons.

The upper (seabed reflection) and lower boundaries of the horizon are two essential parts that have to be picked up and

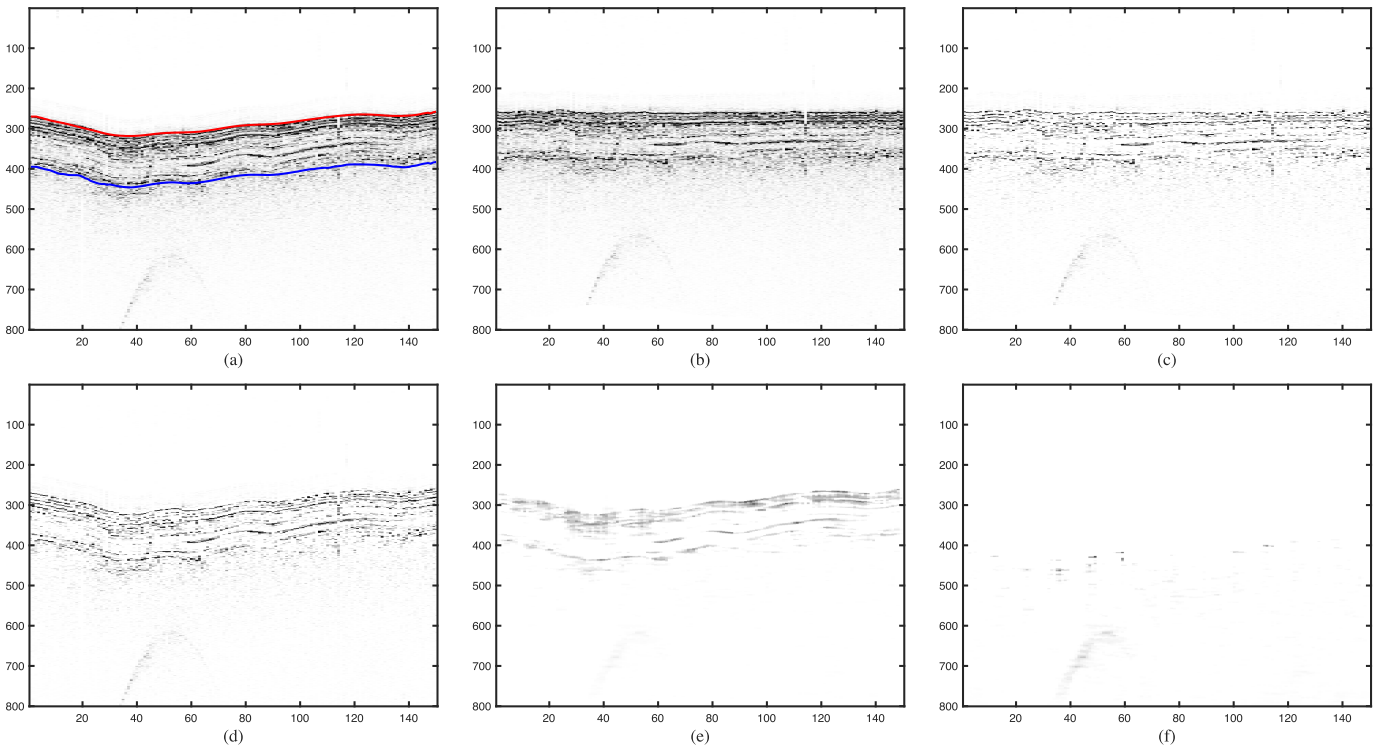


Fig. 4. Illustration of the application of the proposed preprocessing on real data. (a) Input the image with the upper (the red line) and lower (the blue line) boundaries of the horizon. (b) Flattened image. (c) SVD-denoised flattened image. (d) SVD-denoised reconstructed image. (e) Image processed with a median filter. (f) Image after preprocessing.

used as references for subsequent operations in preprocessing. The edge detector is an appropriate method to pick up the horizon. In seismic-like image processing, Sobel, Prewitt, and Roberts are three frequent conventional edge detectors [21]. The Roberts detector is selected because it outlines the continuity of the horizon better than the other detectors. The red and blue lines in Fig. 4(a) are the upper and lower boundaries of the horizon picked up by using the Roberts detector.

Beneath the horizons, a common feature for SBP images is that they contain noise due to the backscattering of microscale scatterers at the interface. The minimum depth of the seabed reflection is looked up as the reference depth. Then, the SBP data are shifted vertically to align the reference depth. The rugged seabed becomes flattened by shifting, as shown in Fig. 4(b). Since backscattering is the interface-correlated noise, it shows a significant linear correlation in the flattened data. The singular value decomposition (SVD) denoise approach is applied to the flattened data to attenuate the backscattering [22]. Afterward, the SVD-denoise flattened data are reconstructed based on the original horizon, thereby obtaining the backscattering suppressed image. Fig. 4(c) and (d) shows the SVD-denoised flattened and reconstructed data, respectively. Additionally, the median filter is employed to attenuate the background noise, as shown in Fig. 4(e).

As the final preprocessing step, the data within the upper and lower boundaries of the horizon are removed from the SBP image. According to Kirchhoff's summary of the Huygens–Fresnel principle, the SBP image can be regarded as a stack of hyperbolas produced by a finite number of scattering points [5]. Therefore, with the successive horizons

being removed, only hyperbola-shaped signatures can change a series of continuous pixels in the image, which is the fundamental assumption of our detection task. The preprocessing result is shown in Fig. 4(f).

C. Image Segmentation

Image segmentation is the process of distinguishing between the signatures and the background, allowing us to focus subsequent processing on the signatures. Some algorithms achieve automatic segmentation by setting thresholds based on the global or local properties of the image [23], [24], [25]. It can be concluded from previous studies that the continuity-based approach is better for SBP image [20], [26].

We present a flood-fill-based method to implement the image segmentation, which can provide better continuity of the signature [27]. In this work, the algorithm requires a level of similarity ρ and a preset background point to act as a seed pixel. The level of similarity is a fraction ρ ($0 < \rho < 1$). We can obtain a threshold by multiplying the ρ by the maximum value of the image. The seed pixel is set as close as possible to the image boundary and has a small value.

The algorithm starts from the seed pixel. At first, the seed pixel visits its connected region. If the pixel value in this connected region is less than the threshold, the pixel is marked as background and used as a new seed pixel; otherwise, the pixel is determined as a signature pixel. The above process is repeated for new seed pixels until the entire image is explored. Further experiments on the level of similarity ρ determination with detailed statistics can be found in Section III-C. The procedure converts the image into a binary image by the flood-fill-based method [see Fig. 5(a)].

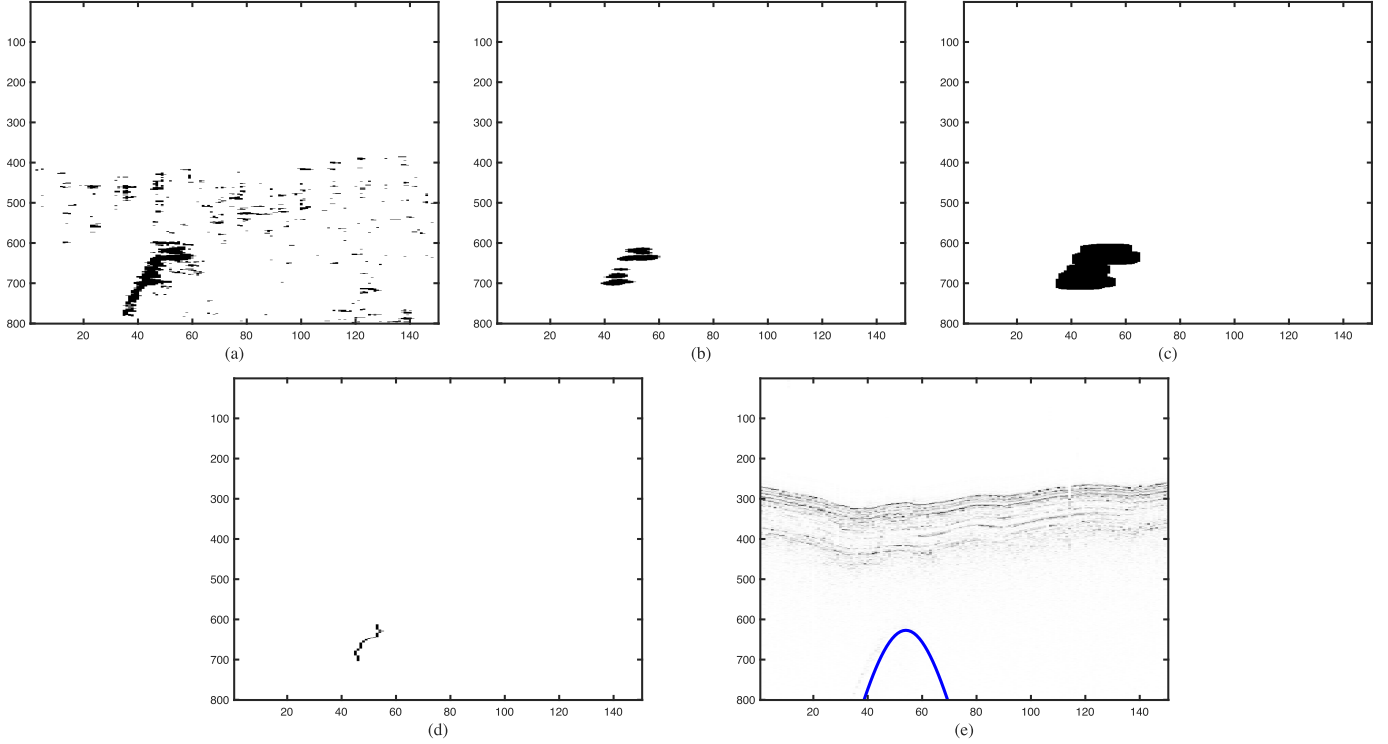


Fig. 5. Illustration of the application of the morphology operations. (a) Result after segmentation. (b) Result after the opening operation. (c) Result after the dilation operation. (d) One-pixel wide curve line reduced from the connected region by skeletonization. (e) Final hyperbolas fit by Levenberg–Marquardt algorithm.

Since the visit process stops at the contour of the signature, our method retains the points enclosed by the signature contour even though these points may be less than the threshold. Thus, it has the advantage of providing better continuity of the signatures.

D. Morphological Processing

Morphological processing is a set of operations that deal with the shape or morphology of features in an image [28]. Our method applies three morphological operations: opening, dilation, and skeletonization.

In our method, two operations are used first: opening and dilation. The opening operation can further remove the irrelevant signals remaining after preprocessing. Then, the dilation operation enables the fragmented ill-shaped hyperbolas to be integrated. At last, skeletonization reduces the hyperbola-shaped signature to a 1-pixel wide trend curve.

First of all, it is necessary to clarify some concepts to explain morphological operations clearly.

Structuring Element (SE): It can be any shape used to determine the neighborhood of a pixel. In our method, the opening operation uses a disk as the SE, and the dilation operation uses a rectangle.

Dilation: The dilation of input image (**IM**) by SE, denoted as **IM** \oplus SE. The dilation operation is to expand the neighborhood range of each valid pixel point (value is nonzero) in the binary image based on the SE.

Erosion: The erosion of **IM** by SE, denoted as **IM** \ominus SE. In contrast to dilation, the erosion operation uses an SE for shrinking the shapes contained in the **IM**.

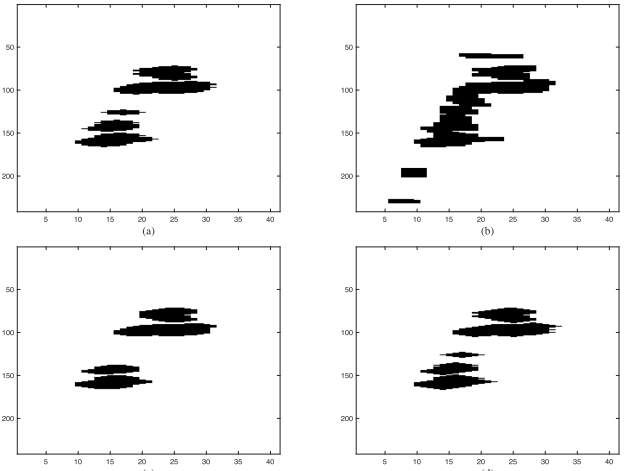


Fig. 6. Performance comparison between the disk-shaped SE and other SEs. (a) Result of disk-shaped SE. (b) Result of square-shaped SE. (c) Result of octagon-shaped SE. (d) Result of diamond-shaped SE.

Opening: The opening operation of **IM** by SE, denoted as **IM** \circ SE, is defined as: **IM** \circ SE = (**IM** \ominus SE) \oplus SE. The opening operation is the combination of dilation and erosion, which filters out noises that are smaller than the SE region while keeping the size of the target feature.

Skeletonization: This operation reduces all the objects in a binary image to a 1-pixel wide curve without changing the fundamental structure of the image.

Fig. 5(b) shows the result after the opening operation. The SE of this operation is a disk with a pixel radius of 3. Some residual noise from preprocessing is filtered out. As shown

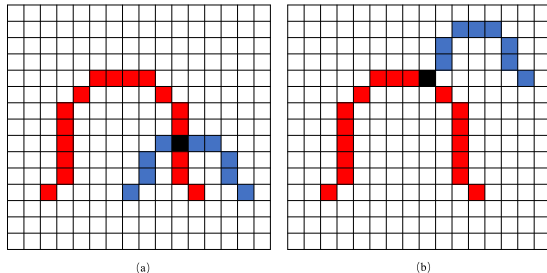


Fig. 7. Illustration of multiple curve crossings. (a) Branch point has four points in its neighborhood. (b) Branch point has three points in its neighborhood.

in Fig. 5(c), the fragmented segmentation results are adjusted into a connected region through dilation. In the operation, the **SE** becomes a rectangle with an axial pixel length of 20 and a lateral one of 10.

It is essential to note that the **SE** selected for the opening and dilation operation are different.

The purpose of the open operation is to filter out artifacts that usually appear as small structures in the binary image, so the structure elements are chosen to prefer a small shape. In addition, the opening operation with a spatially uniform distribution shape helps remove edge spikes and smooth edges; hence, a disk is defined as an **SE** in this operation. We compare the performance of the disk-shaped **SE** with other **SE** shapes, as depicted in Fig. 6. For all comparisons, the pixel values of our input parameters are set to 3 to generate the **SE**. Fig. 6(a) illustrates the results of the disk-shaped **SE**, effectively smoothing the edges of the connected region and filtering out irrelevant structures. In contrast, Fig. 6(b) demonstrates that the square-shaped **SE** is unsuitable for our workflow, being more suited for processing grid-like structures. Fig. 6(c) shows that the octagon-shaped **SE** provides superior edge-smoothing effects. However, when selecting a size, the octagon-shaped **SE** is only selectable in multiples of 3, which restricts flexibility in **SE** size selection. Given the small **SE** sizes used in the proposed method, both the disk and diamond-shaped **SE** are interchangeable. Nevertheless, the diamond-shaped **SE** may introduce elongated shapes, as shown in Fig. 6(d).

The dilation operation in our method is crucial in recovering the shape of hyperbolas, which enables the fragmented ill-shaped hyperbolas to be integrated. If a suitable **SE** can be selected to allow the hyperbola-shaped signature to become a connected region, further processing can be simplified. At this stage, the connected regions assist in roughly locating the local perturbations corresponding to the signatures. In this work, the gap between lateral and axial resolutions is the main factor that corrupts the continuity of the signature. Therefore, we suggest that an axially dominant shape is used for **SE**.

Then, skeletonization reduces the connected region to a 1-pixel curve. While there are many ways to implement skeletonization, a four-connectivity function is selected since the removal of excrescent skeletal branches [27]. The trend curve of the original hyperbola-shaped signature can be obtained using skeletonization, which is displayed in Fig. 5(d).

It is common for the signatures to cross in SBP images, so we have to distinguish multiple connected signatures.

In mathematical morphology, trend curves are formed by monotonic curves defined as branches. These branches are connected, and their connection points are called branch points. In both subfigures of Fig. 7, the black pixels dot indicate the branch points. The number of branches crossed is obtained by dividing the number of points in the neighborhood (8 pixels around the pixel) of the branch point by 2. The number is then rounded up.

The branch point in Fig. 7(a) has four points in its neighborhood, so two curves cross. The direction of the lines corresponding to these four points is then used as a constraint to distinguish between two curves, each represented by a different color in the figure (a blue line and a red line). Similarly, the curves in Fig. 7(b) can be distinguished, but the unique feature is that we only need to determine the direction of one curve. It is uncommon for more than two hyperbola-shaped signatures to cross in field data, as interference between multiple point scatterers reduces the overall amplitude and makes it difficult to detect.

E. Fitting Algorithm

The trend curve provided by skeletonization can outline the shape of the signature, but more refined results require further fitting. The 1-pixel feature permits us to implement the fitting algorithm using the least-squares method

$$\underset{a,b}{\operatorname{argmin}} \|t(x) - \phi(x)\|_2^2 \quad (4)$$

where $\phi(x)$ is the curve corresponding the morphological trend of a hyperbola-shaped signature, and $t(x)$ can be calculated by (3), which can be rewritten as

$$t(x) = \sqrt{a^2 \left[1 + \frac{(x - x_0)^2}{b} \right]}. \quad (5)$$

Although three unknown parameters need to be calculated, x_0 can be determined by the peak of the trend curve.

Many algorithms have been dedicated to solving this nonlinear least-squares problem [29]. This work employs the Levenberg–Marquardt algorithm to fit the hyperbolas due to its robustness [30]. In many cases, the algorithm can find a solution even if it starts far off the final minimum. Therefore, although the trend curves of some ill-shaped signatures lack parts of the hyperbola branches, the method can calculate the unknown parameters of (5). By using the trend curve in Fig. 5(d) as a fitting object, the final fit of the original image Fig. 3 is plotted in Fig. 5(e). The domain of the definition of the fitting result is determined by the connected region obtained by the dilation operation. If the signature is ill-shaped, we complement its shape based on its symmetry.

III. EXPERIMENTS

A. Dataset

In this article, the data source is the 2006 cruise mission, which aims to map the western insular margin and 2500-m isobath of Guam and the Northern Mariana Islands. The acquisition device is a Knudsen 320B/R chirp 3.5-kHz high-resolution echosounder [31]. The image was acquired in the vicinity of the Western Mariana Ridge. Numerous guyots,

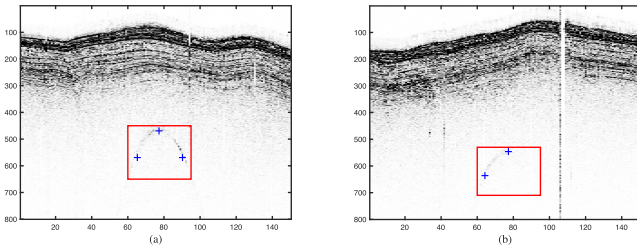


Fig. 8. Example of ground truth in SBP images. The red rectangles are the ROI containing the signature, and the blue “+” signs in the images are feature points. (a) Standard signature. (b) Ill-shaped signature.

cross-chain volcanoes, and other anomalous intrusion structures exist in this region [32], [33]. Potential magmatism provides a large number of hyperbola-shaped signatures in this data.

The fitting algorithm produces an analytical curve that enables us to quantitatively determine the geometric parameters of the hyperbola-shaped signatures. First and foremost, the vertex of the hyperbolas is the most valuable and obvious information, which locates the point scatterers. In the fitting, we assume that the peak of trend curves is the vertex of hyperbolas. The assumption does not entirely avoid fitting bias, but it ensures that the prediction of the vertex on the x -axis is relatively accurate, at least.

Given that the velocity parameter is typically assumed constant in SBP images, the fit parameter plays a crucial role in calculating the physical size of the point scatterers. The geometry of the SE is chosen to be as small as possible in both the opening and dilation operations to prevent disruption to the geometric trend of the signatures. As a result, skeletonization correctly maps the trend curve from the original image, thus completing the fitting of the analytical curve.

The location and physical size of the point scatterers can help us quantitatively analyze magmatism activity in the exploration area.

B. Experimental Setup

The feature points of the hyperbola method are employed to evaluate the performance referring to [10]. For each hyperbola in the field data, three feature points are marked manually: the vertex, a point on the left side of the vertex, and another point on the right side [see Fig. 8(a)]. The vertex is essential, whereas the other two points can be retained as just one if a signature is ill-shaped [see Fig. 8(b)].

For each fit hyperbola in images, if the group of points is found with an average distance to the hyperbola of fewer than 10 pixels in axial and 5 pixels in lateral, this hyperbola is regarded as a true positive; otherwise, it is taken as a false positive. The red rectangles mark the region, including hyperbolas, for better readability. These regions can also be considered as ROIs that contain hyperbolas.

The method provides two quantization results: recall and precision. The recall and precision can be calculated

$$\text{Recall} = \frac{t_p}{t_p + f_n} \quad (6)$$

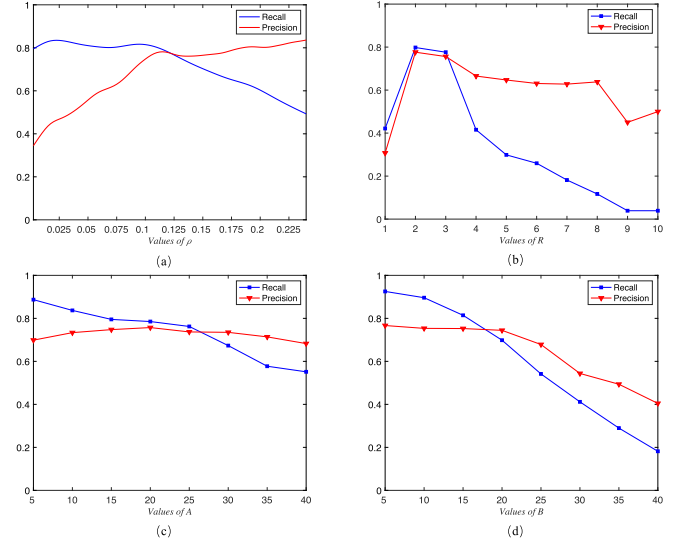


Fig. 9. Illustration of the effect of the parameters on the values of recall and precision of detection when using the proposed method on a group of SBP images. (a) Effect of the level of similarity ρ . (b) Radius of disk-shaped SE in the opening operation R . (c) Size of SE in the dilation operation A . (d) Size of SE in the dilation operation B .

$$\text{Precision} = \frac{t_p}{t_p + f_p} \quad (7)$$

where t_p is the number of true positives; f_n (false negative) is the number of missed hyperbolas in the ground truth; and f_p (false positive) is the number of detected hyperbolas, which are not included in the ground truth. Based on these results, we can further discuss the performance of the proposed method.

Since the signatures in the field data are not uniformly distributed, 64 suitable images are cut out for experimental purposes. The configuration of each picture is consistent. Their size is 800×150 , the axial direction resolution is 0.3125 m, and the lateral direction is 40 m. The images contain hyperbola-shaped signatures at different depths. Some signatures are clear and well-shaped, while the others are to some extent indistinct and misshapen. The ground truth is that 152 hyperbolas are manually labeled from these images.

C. Thresholds Determination

The level of similarity ρ , the size of SE in dilation, and opening operation play an essential role in the detection performance. Hence, experiments were carried out to determine their value. All experiments are independent of each other. To avoid experiments influenced by other parameters, we adjusted parameters besides the evaluated thresholds to optimal values before each experiment.

The first experiment was designed to determine the range of ρ on the datasets. Fig. 9(a) shows that recall decreases while precision increases with the value increase of ρ . When ρ is 0.124, the two evaluation curves intersect, and both recall and precision are 0.781, which is an acceptable value. With this as a reference, $[0.1, 0.125]$ is selected as the range of ρ in our experiments.

Similar to the first experiment, we tested a range of R , which is the radius of disk-shaped SE in the opening operation. As shown in Fig. 9(b), it can be seen that both recall and precision perform better in the opening operation when the

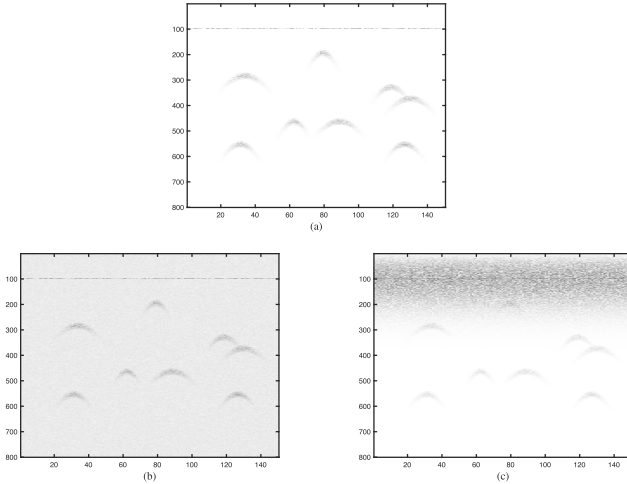


Fig. 10. Example of different types of synthetic images. (a) Synthetic image. (b) Synthetic image with Gaussian white noise. (c) Synthetic image with backscattering.

value of R is 2 or 3 of disk-shaped SE, while recall decreases rapidly with the value greater than 3. Other shapes have been tested with similar SE areas using optimal parameters. Compared to other shapes, disk-shaped SE enables a decrease in branches from skeletonization to obtain better precision.

The effect of the size of SE in the dilation on the values of recall and precision of detection using the proposed method on a group of SBP images is illustrated in Fig. 9(c) and (d). A and B correspond to the axial and lateral sides of the rectangle, respectively. The precision of A yields a good performance at a value of about 20, while the recall decreases as the value increases in the range. In this experiment, the preset value of B is 10. Our experiment chooses an optimal range for A, which is [15, 25] to balance the precision and recall. Both precision and recall decrease with the growth of B. In the experiment of determining B, the preset value of A is 20, and it can be seen in Fig. 9(d) that the curve can no longer guarantee sufficient precision and recall when B is greater than 20. Therefore, we suggest that the SE of dilatation should be an axially dominant rectangle.

Overall, the optimal range for ρ and A are [0.1, 0.125] and [15, 25], respectively. The value of B should be smaller than A to achieve its best performance. The value of R should be set to 2 or 3. The combination of precision and recall determines the thresholds. However, for some interpreters, precision is more important than recall since picking an incorrect result is less tolerable than missing a signature to them. Therefore, ρ and B could be adjusted appropriately to improve accuracy.

D. Synthetic Data

We apply the proposed algorithm to synthetic datasets to analyze the effect of the noise. The synthetic datasets are generated to simulate the hyperbola-shaped signatures with different curvatures using the convolutional model according to Zheng et al. [9], as shown in Fig. 10(a). The amplitude of the signal ranges from 0 to 1. A straight line located at 100 on the y-axis is assumed to be a reflective interface that can be regarded as the seabed, which is essential for the modeling of backscattering. The amplitude of this reflective interface is set

to 3. Actually, the difference in amplitude between the seabed and the signature in the real data is more than a factor of 10. A matrix of random attenuation coefficients is applied to simulate the energy loss of the signal.

Background noise and backscattering are the two types of noise we analyze. They can all be assumed to be additive noise. We use Gaussian white noise to simulate the background noise, as shown in Fig. 10(b). The signal-to-noise ratio of Fig. 10(b) is 2 dB. Based on the assumption of Zhao et al. [20], we use the Rayleigh distribution to assume the energy distribution of the noise on a ping for the modeling of backscattering, as shown in Fig. 10(c). The location of the seafloor assists us in determining the input parameters of the Rayleigh distribution function. To make the noise more consistent with the randomness of the diffuse reflections, we make a random distribution attenuation on the signal energy.

We simulate 200 signatures to test the precision and recall of the proposed method. Even if the signal-to-noise ratio of the images with Gaussian white noise is as low as 0.1 dB, the precision and recall of our method are above 90%. Therefore, we consider that background noise is not a major factor affecting the proposed method.

In images with backscattering, only signals below 220 on the y-axis can be detected because the amplitude of backscattering starts to be less than 1 at 220 on the y-axis. Backscattering is the reflection from the microscale topography of the interface. According to our previous assumptions, the signal energy of backscattering is high close to the interface and then decreases rapidly within an interval. Consequently, backscattering generates a shadow-like region beneath the seafloor interface. The proposed method, without denoising, struggles to detect the signature in this region because the noise amplitude may be larger than the signature. However, with a denoising step, our method may suppress both the signature and noise. Overall, the proposed method is effective when the amplitude of the backscattering is less than the signature, and the background noise has little effect on the proposed method.

E. Real Data

We select two representative SBP images to present our results and validate the feasibility of the proposed method. Figs. 11(a) and 12(a) show SBP images with ground truth, and Figs. 11(b) and 12(b) show corresponding results by using the proposed method. The blue curves in Figs. 11(b) and 12(b) are the hyperbolas, which are detected by using the proposed method. The ROIs of each ground truth are labeled to describe our results better. In these two experiments, we use the following parameters: ρ is 0.125, R is 2, A is 25, and B is 10.

In Fig. 11(a), there is a well-shaped signature containing three feature points in its ROI (signature 1). The other signatures are ill-shaped, providing only two feature points (signatures 2–4). The overall amplitudes of signatures 3 and 4 are much smaller than the well-shaped ones. Thus, the segmentation results of these signatures do not demonstrate good continuity, as shown in Fig. 11(c). In Fig. 11(d), these weak signatures are processed into connected regions by

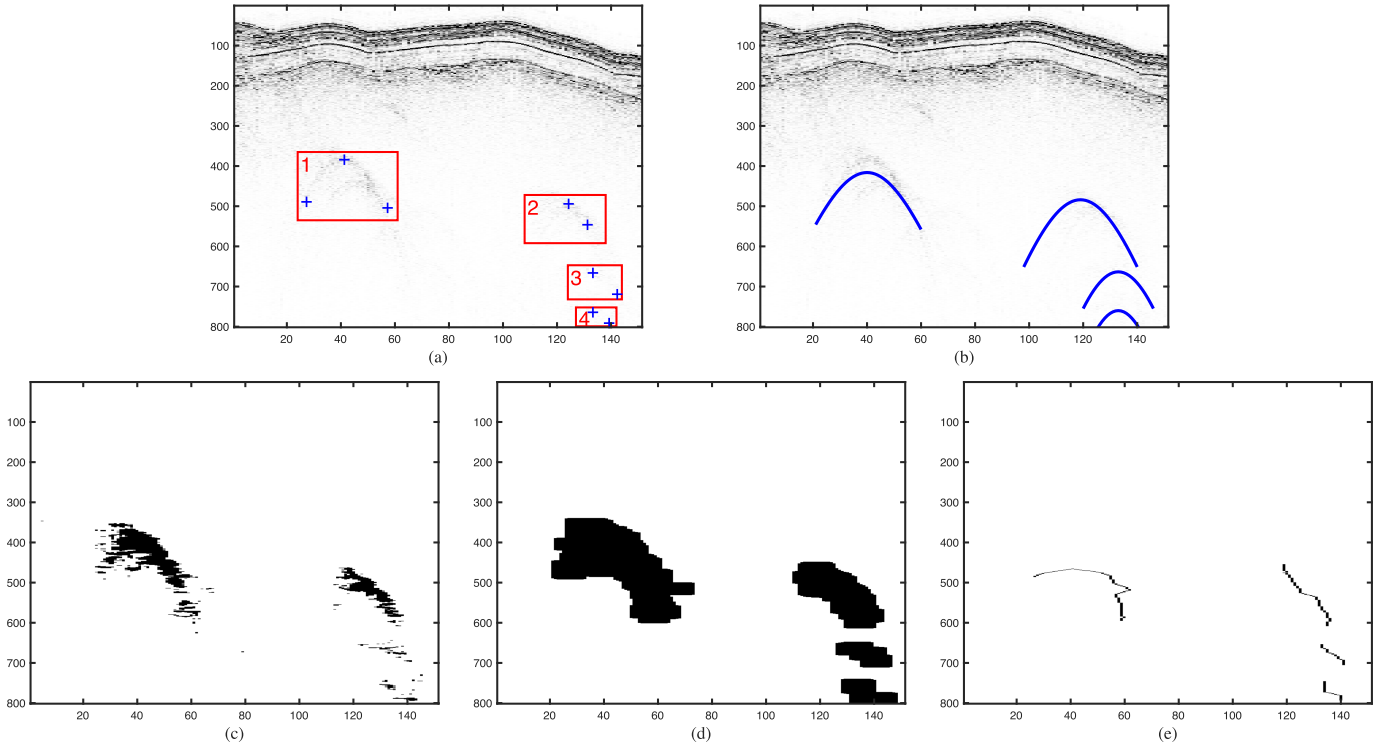


Fig. 11. Illustration of the application of the proposed method on the first field SBP image. (a) Input image with ground truth. (b) Output image. (c) Image after segmentation. (d) Result after morphology processing. (e) Trend curves reduced from the connected region by skeletonization.

TABLE I
COMPARISON OF THE DETECTION RATES AND FITTING
RATES AMONG DIFFERENT METHODS

Method	Precision	Recall	Time(s)
The proposed method	0.754	0.811	1.9
C3 method	0.060	0.102	0.6
Canny+Li et al. method	0.429	0.379	1.1

morphological operations. After skeletonization, the connected regions are simplified into trend curves. Since signatures 2–4 are ill-shaped, their trend curves are incomplete [see Fig. 11(e)]. Fig. 11(b) shows the final result of the fit using the Levenberg–Marquardt algorithm. According to our evaluation method, the proposed method can detect all signatures in Fig. 11(a) with no missed and false detections.

Fig. 12(a) shows an example containing signatures with significant differences in curvature. Beyond that, two features are cross-linked (signatures 1 and 2). The processing of the proposed method is independent of curvature. As shown in Fig. 12(c) and (d), these signatures with different curvatures can be segmented and then processed into connected regions by morphological operations. The trend curves in Fig. 12(e) provide a typical case of intersection. Using the proposed distinguishing method, the trend curves of signatures 2 and 3 can be distinguished and fit separately. In Fig. 12(e), the trend curves provided by their morphological processing may differ slightly from the real trend curves of the signatures. However, although the fitting result of signature 3 is slightly deviated, these differences are within the error range of our evaluation method (an average distance of the ground truth to the hyperbola of fewer than 10 pixels in axial and 5 pixels in lateral).

There appears to be another signature that needs to be labeled in the upper right corner of signature 2. It is not a signature but an artifact resulting from a shadow-like region. This artifact affects our detection result, as it shifts the fit hyperbola upward overall. The differences are also within the error range of our mentioned evaluation method. Dealing with the shadow-like region is indeed a tricky technical bottleneck, which we discuss in more detail in Section IV-D.

At last, we tested the proposed method on our image dataset. As shown in the first row of Table I, the precision and recall can achieve more than 75% and 80%, respectively.

F. Performance Comparison

We compared the performance of the proposed method with the methods introduced by Dou et al. [10] and Li et al. [8] on the field datasets. Dou et al. [10] proposed the column-connection clustering (C3) method to detect the hyperbolas in GPR images. Although the SBP devices are fundamentally different from GPR, we suggested the C3 method has significance for hyperbolas detection. We employed the C3 method procedure directly on our dataset to determine whether the methods applied to GPR can be directly transferred to SBP images. As presented in Li et al. [8], the edges are picked with a comprehensive edge extraction and then use the theoretical hyperbola with a buffer zone to match the signatures. In their method, the instantaneous phase must be used to enhance the edges, but for the SBP devices used by us, no phase information is provided. Thus, we have to apply the Canny edge detection algorithm to replace their edge extraction method. The Canny algorithm is also standard in some studies [13], [14]. The

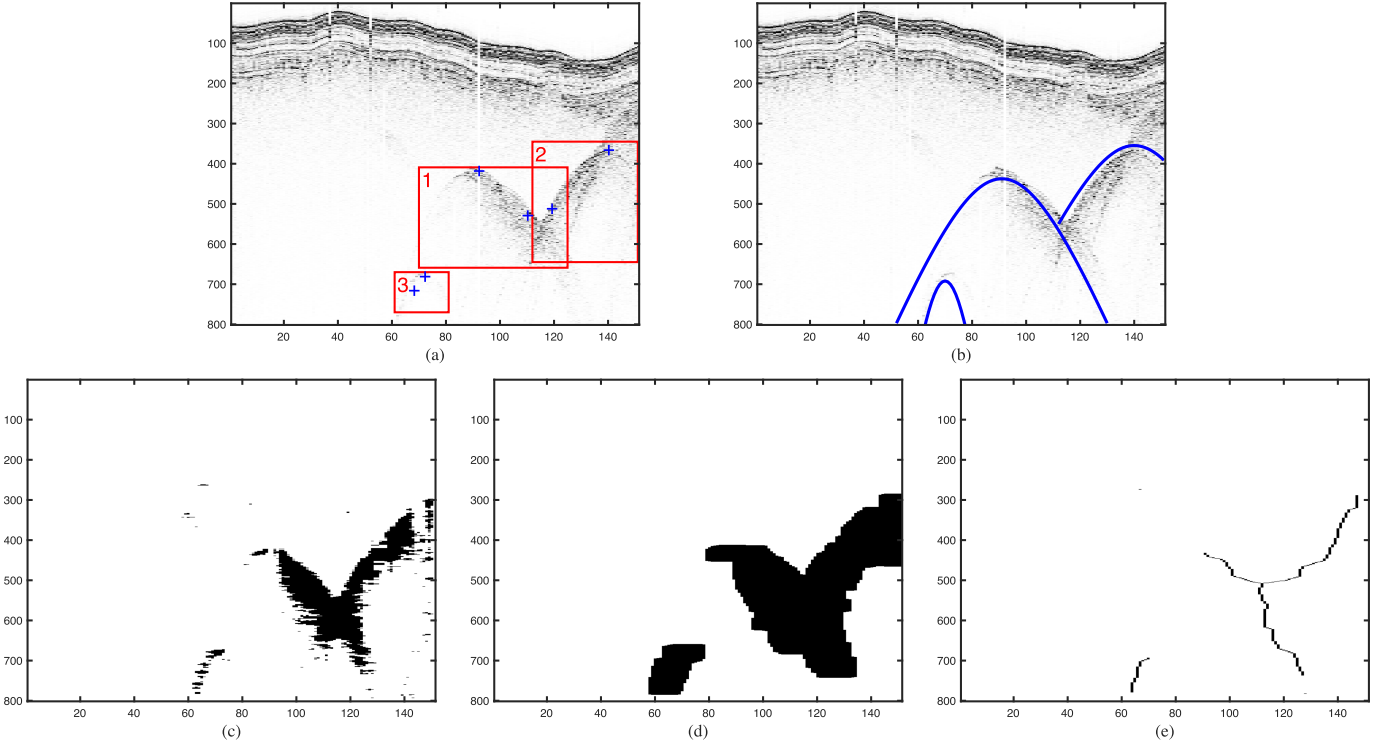


Fig. 12. Illustration of the application of the proposed method on the second field SBP image. (a) Input image with ground truth. (b) Output image. (c) Image after segmentation. (d) Result after morphology processing. (e) Trend curves reduced from the connected region by skeletonization.

templates are set up regarding to Zheng et al. [9], as shown in Fig. 2(c).

A complex case containing more signatures is selected to compare the performance of the hyperbola-shaped signature detection methods, as shown in Fig. 13(a). In Fig. 13(b), six signatures can be detected by applying the proposed method. In this experiment, we use the following parameters: ρ is 0.125, R is 2, A is 15, and B is 8. These signatures contain weak signals and have varying curvatures. Fig. 13(c) shows the result detected by the C3 method. Only signature 5 is detected in the image. The overall amplitude of signature 5 is the largest of these signatures. As shown in Fig. 13(d), the template matching method can detect three signatures. This method seems to detect some signatures that cross together as one, such as signatures 3 and 4. Signatures 3 and 4 are two ill-shaped signatures, one missing the left branch and the other missing the right branch. However, after carefully inspecting the left branch of signature 4, we consider that there was still a signal with weak amplitude on the left side. Signature 4 can be considered as an independent signature. The same thing happens with signatures 5 and 6. The template matching method may detect some crossed ill-shaped signatures into one signature.

We test both methods on our image dataset. The precision and recall rates of the correctly fit hyperbola from different methods are shown in the second and third rows of Table I. Compared with the C3 and Li et al. [8] methods, the proposed method demonstrates better precision and recall in the geology survey data. Therefore, we suggested that the proposed method is effective in detecting the hyperbola-shaped signature in SBP images. Besides, we compared the computational cost of

these algorithms. The computation times for each algorithm on individual images are presented in the third column of Table I. The hardware platform is Apple M1 Max CPU and 32 GB of host memory. The software platform is macOS Sonoma. The MATLAB 2021b is adopted for implementing all the algorithms. Based on the experimental tests, all three algorithms demonstrate the capability to achieve real-time interpretation in practical scenarios. Compared to the other two methods, the proposed method includes an additional algorithm for least-squares fitting, resulting in slightly longer computation times.

IV. DISCUSSION

A. Parameters Determination

In our experiment, we present the optimal parameters that fit the field data. Nevertheless, suitable modification should be made on these parameters depending on the sonar instrument or application scenario. In Table II, we list some of the factors that would affect the parameters. These items are quite representative although they are not comprehensive. ρ is a parameter that needs to be set carefully, as segmentation is the basis of the proposed method. The parameters of morphology operation are used for determining the size of SEs: the radius R and a pair of lengths A and B . The radius R serves as the opening operation to define the size of the disk. It must be a small value; otherwise, SE would break the continuity of the target shape. Our experiments show that the recall value is significantly impacted when R is too large. We verified experimentally that the SE in the dilation operation should be an axially dominant shape.

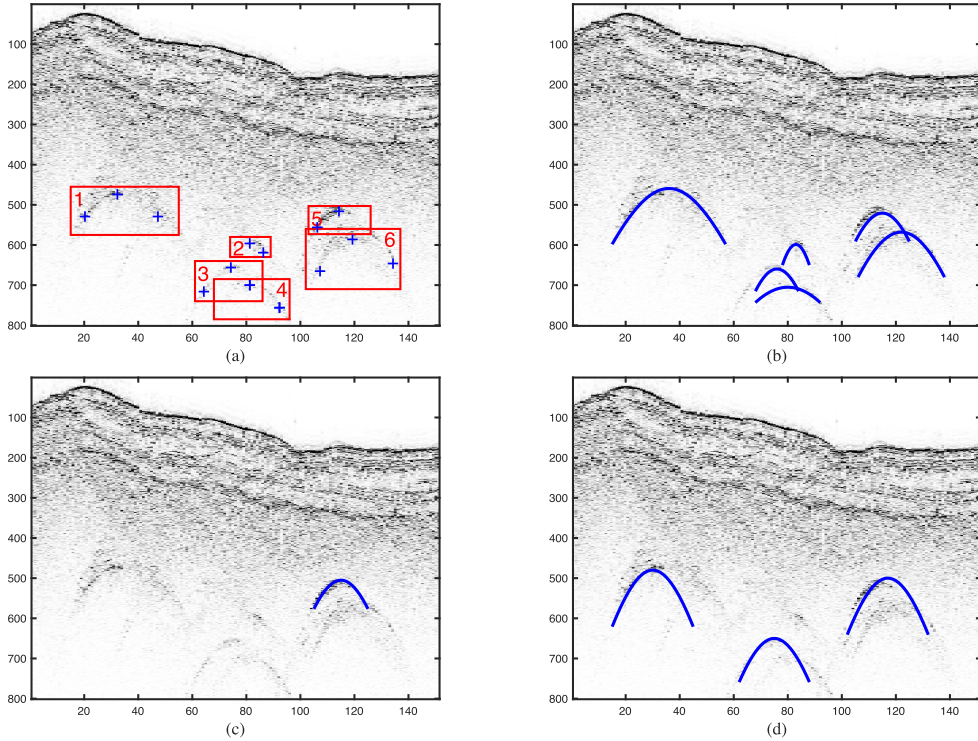


Fig. 13. Performance comparison between the proposed method and other methods. (a) Input image with ground truth. (b) Result of the proposed method. (c) Result of the C3 method. (d) Result of the template matching method.

TABLE II
FACTORS AFFECTING THE SELECTION
OF PARAMETERS

Parameter	Influence factor
ρ	Subsurface media properties; Device settings (sample frequency, amplitude etc.); Propagation losses.
R	Subsurface media properties; Noise intensity.
A,B	Subsurface media properties; Acquisition mode; Device settings; Propagation losses.

After obtaining the optimized parameters, we further analyzed the performance of the proposed method. As depicted in Figs. 11 and 12, we validated the feasibility of the proposed method to detect the ill- and well-shaped hyperbolas. Meanwhile, although the signatures in the SBP image have significant differences in curvature, the proposed method can detect all of them. We also test the proposed method on the image dataset. Overall, the rate of precision and recall are satisfactory. For field data, we suggest that the recall of 80% would indicate that our detection results cover the majority of hyperbola-shaped signatures.

The proposed method necessitates reference to empirical parameter intervals to achieve optimal parameter settings before application, which exhibits a slight gap compared to the point-and-shoot approaches. These parameters can be derived through an adaptive parameter optimization strategy considering device settings and acquisition modes. While theoretically feasible, this strategy requires complex modeling, rigorous theoretical support, and validation across multiple scenarios in practice. As data collection costs decrease, we suggest that a data-driven optimization method may be viable [34]. The data-driven approach focuses on mining data patterns and trends

within extensive datasets, aiming to derive optimal parameters effectively. We will explore integrating a data-driven approach into our future research efforts to move toward achieving a fully automated detection workflow.

B. Morphological Processing

Morphological processing constitutes a central technique in the proposed method, modifying the shape and structure of objects in images based on the properties of predefined SEs. To address the peculiarities of SBP images, we employ the opening and dilation operations to improve the continuity of detected target regions.

In the field data, we verified that it is possible to use morphological operations that can restore the morphology of the signature. Indeed, the critical factor in ensuring the effectiveness of morphological operations lies in selecting the appropriate SEs. We implement morphological operations using generic SEs. This approach simplifies implementation and avoids the complexities of imposing physical constraints. However, using generic SEs may cause the trend curve obtained after skeletonization to deviate from the true signature, resulting in subjective and potentially insufficient fits.

In the opening operation, we employ a disk for its ability to effectively remove irrelevant signals, such as backscattering, without assumptions about their statistical distribution. Backscattering signals can sometimes exceed the energy of hyperbolic-shaped signatures, leading to segmentation revealing numerous small structures, as shown in Fig. 5(a).

In dilation operation, the use of a rectangular SE, while enhancing lateral and axial resolutions, compromises method stability. It may roughen mask edges, causing deviations in

the trend curve after skeletonization. Therefore, introducing constraints in the dilation operation is crucial to align the mask with the original signature. An adaptive SE incorporating amplitude and physical constraints could potentially resolve this issue (see [35]). Future research will explore integrating adaptive SEs to enhance method stability and accuracy. Additionally, incorporating original data amplitude as a constraint in skeletonization algorithms aims to better align trend curve results with manual interpretation.

C. Performance Comparison

Although the proposed method provides results consistent with ground truth, comparison with other methods is essential. We provide a complex case to compare the performance of different methods, as shown in Fig. 13. The C3 method is a developed workflow. Our initial intention is to see if the GPR method could be transported to the SBP images, so we did not see the need to adapt it too much and apply it directly. It may be unsuitable to directly apply the methods that work on the GPR images to manage the SBP images since precision and recall are under 10%. Generally, some researchers use unique techniques to improve the segmentation results of the GPR images.

In previous studies, template matching was the most commonly used method. These methods provide more robust and precise results with specific targets, making them efficient for artificially buried objects. The fact that template matching method can also provide a result, which can basically meet interpretation requirements. In geological surveys, the shape of the target requiring identification, such as magmatic intrusions, is more complex and irregular. Thus, the template is challenging to cover all the signatures. The issue of edge extraction is mentioned in [8], where the Canny algorithm needs to provide better results. However, the Canny algorithm is a reluctantly appropriate option for our data. The conditions and scenarios for using our method are much more general because, in geological interpretation, the interpreter can generally only obtain the SBP images composed of instantaneous amplitudes. Li et al. [8] proposed a method to get the edge information using the instantaneous phases, and geological interpreters generally need help to satisfy such prerequisites. Even after replacing the dataset, if the instantaneous phase is unavailable, we still need help fulfilling the requirements of the Li et al. [8] method. Furthermore, the Canny operator maximizes the fulfillment of the prerequisites required by the Li et al. [8] method. The Canny algorithm and an incomplete template database may cause some signatures to be missed. It is worth noting that the template matching method sometimes fails to fit the hyperbola with irregular shapes or large curvatures. The method detects some crossed ill-shaped signatures as one signature [see Fig. 13(d)]. In SBP images, it is common for multiple ill-shaped signatures to cross.

The proposed method does not require the constraints of a priori knowledge. As our basic assumption provided in Section II-B, any connected region with better continuity in the image can be considered as a candidate for signature after preprocessing. The hyperbola is then obtained by skeletonizing these connected regions. The proposed method

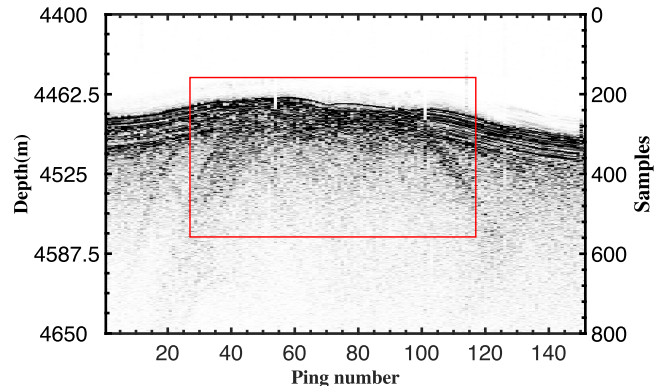


Fig. 14. Shadow-like region in the SBP image.

does not distinguish whether the monotonicity of the skeletonized curve meets the hyperbolas. Therefore, it enables well- or ill-shaped signatures to be detected. In addition, the proposed method considers the case of multiple curve crossings. In conclusion, the proposed method can effectively detect the hyperbola-shaped signatures in the SBP images.

D. Shadow-Like Regions

We check the results of some of the false positives. Some shadow-like regions close to the horizon are also detected. The prerequisite of applying the proposed method is that preprocessing can clean up the vast majority of extraneous information, including horizon and noise. Hence, a more complex preprocessing procedure is required for the data with low quality to segment the ROI of the signature. In field data, the sediment medium on the seafloor is not uniformly distributed. The sediment has a more acoustic impedance in some localized areas, resulting in relatively thin acoustic penetration depths. However, the acoustic wave energy excited by the sonar is consistent. Hence, there is backscattered solid noise beneath these high acoustic impedance interfaces. The visualization of the noise in the image is that a shadow-like region will appear, as shown by the red box mark in Fig. 14. These shadows are also segmented in the proposed method, while they are not part of the horizon. Therefore, they are not removed. Some false detections picked up these shadows incorrectly as hyperbola-shaped signatures. We suggest that this problem can be solved by complex denoising methods or by using the global acoustic penetration depth as a constraint. These, however, are not the focus of this article, and we may discuss this issue in a later study.

E. Method Integration With Deep Learning

It is well worth mentioning that deep learning approaches have been widely used in hyperbola-shaped signature detection in GPR data [16]. Since the mode of SBP devices is similar to that of GPR, we suggest that deep learning-based detection methods may also have good prospects for SBP data. In [9], the end-to-end deep learning was verified for pipeline detection with a fixed curvature hyperbola-shaped signature in the SBP sonar image. Deep learning models typically require large amounts of labeled signatures for training purposes. For some geological surveys, complex subsurface targets make acquiring

such signatures challenging and may require significant manual effort or synthetic data generation.

We suggest that the proposed method fills a niche where rapid label generation for deep learning approaches can be facilitated through morphological processing. After the dilation process, hyperbola-shaped signature masks are available. Signatures can be extracted as data samples based on the masks. The fit hyperbolas will then be used as labels to match the sample. The proposed method-based data label generator can assist deep learning models in directly learning patterns from the field data, thereby enhancing the generalization capability. If the objective is to improve the algorithm for rapid label generation, the algorithm must maintain a higher precision (e.g., 90%), even if the recall decreases significantly. In the previous discussion, we mentioned two techniques that need major improvements, i.e., adaptive parameter optimization and adaptive SE. Both enable the freeing of the proposed methods directly from human intervention while improving precision and stability. Future research could explore synergies between morphological processing and deep learning to further enhance the accuracy and efficiency of hyperbola-shaped signatures detection in SBP sonar images.

V. CONCLUSION

This article has proposed a hyperbola-shaped signature detection method using morphological processing. The method comprises four steps: preprocessing, segmentation, morphological processing, and fitting. The preprocessing aims to filter out signals unrelated to the hyperbola-shaped signatures, which can be achieved using horizon-picking theoretically. Then, the segmentation extracts the pixels of interest from the background. The morphological processing is the critical technology, including opening, dilation, and skeletonization, which can outline the trend curves of well- or ill-shaped hyperbola-shaped signatures without a priori knowledge. The opening operation filters out some small structures that are suggested to be noisy, and the criterion of “small” is measured by a disk-shaped SE. This operation has the additional benefit of not changing the signature area and smoothing the edges. The dilation operation would restore the fragmented signature to a connected region, and the SE of this operation needs to be set according to the resolution. The skeletonization outlines the trend curves of the signature. Finally, the fitting algorithm can further refine the trend curves into an analytical curve.

The experimental results on geological survey data verified the feasibility of the proposed method. Compared with the template matching and the C3 methods, the proposed method can provide better precision and recall and demonstrate superior performance in detecting ill-shaped and large curvature hyperbola-shaped signatures. By suitably modifying the parameters, the morphological operations presented in this article can be used as a generic hyperbola-shaped signature detection module in arbitrary SBP images.

ACKNOWLEDGMENT

The authors would like to thank Doctoral Candidate Yu Tang from Southwest Jiaotong University for her guidance on writing.

REFERENCES

- [1] W. H. Geissler et al., “Seafloor evidence for pre-shield volcanism above the Tristan da Cunha mantle plume,” *Nature Commun.*, vol. 11, no. 1, p. 4543, Sep. 2020.
- [2] D. E. Sawyer, R. Urgeles, and C. L. Iacono, “50,000 yr of recurrent volcanioclastic megabed deposition in the Marsili Basin, Tyrrhenian Sea,” *Geology*, vol. 51, no. 11, pp. 1001–1006, Nov. 2023.
- [3] Y. Chen, B. Deng, G. Zhang, W. Zhang, and S. Gao, “Response of shallow gas-charged Holocene deposits in the Yangtze Delta to meter-scale erosion induced by diminished sediment supply: Increasing greenhouse gas emissions,” *J. Geophys. Res. Earth*, vol. 128, no. 1, 2023, Art. no. e2022JF006631.
- [4] X. Lurton, *An Introduction To Underwater Acoustics: Principles and Applications*, 1st ed., Berlin, Germany: Springer, 2002.
- [5] B. Schwarz, “An introduction to seismic diffraction,” in *Advances in Geophysics*, vol. 60. Amsterdam, The Netherlands: Elsevier, 2019, pp. 1–64.
- [6] M. Guan, Y. Cheng, Q. Li, C. Wang, X. Fang, and J. Yu, “An effective method for submarine buried pipeline detection via multi-sensor data fusion,” *IEEE Access*, vol. 7, pp. 125300–125309, 2019.
- [7] W.-M. Tian, “Integrated method for the detection and location of underwater pipelines,” *Appl. Acoust.*, vol. 69, no. 5, pp. 387–398, May 2008.
- [8] S. Li, J. Zhao, H. Zhang, and Y. Zhang, “Automatic detection of pipelines from sub-bottom profiler sonar images,” *IEEE J. Ocean. Eng.*, vol. 47, no. 2, pp. 417–432, Apr. 2022.
- [9] G. Zheng, J. Zhao, S. Li, and J. Feng, “Zero-shot pipeline detection for sub-bottom profiler data based on imaging principles,” *Remote Sens.*, vol. 13, no. 21, p. 4401, Nov. 2021.
- [10] Q. Dou, L. Wei, D. R. Magee, and A. G. Cohn, “Real-time hyperbola recognition and fitting in GPR data,” *IEEE Trans. Geosci. Remote Sens.*, vol. 55, no. 1, pp. 51–62, Jan. 2017.
- [11] X. Zhou, H. Chen, and J. Li, “An automatic GPR B-scan image interpreting model,” *IEEE Trans. Geosci. Remote Sens.*, vol. 56, no. 6, pp. 3398–3412, Jun. 2018.
- [12] E. Pasolli, F. Melgani, and M. Donelli, “Automatic analysis of GPR images: A pattern-recognition approach,” *IEEE Trans. Geosci. Remote Sens.*, vol. 47, no. 7, pp. 2206–2217, Jul. 2009.
- [13] L. Mertens, R. Persico, L. Matera, and S. Lambot, “Automated detection of reflection hyperbolas in complex GPR images with no a priori knowledge on the medium,” *IEEE Trans. Geosci. Remote Sens.*, vol. 54, no. 1, pp. 580–596, Jan. 2016.
- [14] Ž. Bugarinović, L. Pajewski, A. Ristić, M. Vrtunski, M. Govđedarić, and M. Borisov, “On the introduction of Canny operator in an advanced imaging algorithm for real-time detection of hyperbolas in ground-penetrating radar data,” *Electronics*, vol. 9, no. 3, p. 541, Mar. 2020.
- [15] C. G. Windsor, L. Capineri, and P. Falorni, “A data pair-labeled generalized Hough transform for radar location of buried objects,” *IEEE Geosci. Remote Sens. Lett.*, vol. 11, no. 1, pp. 124–127, Jan. 2014.
- [16] Y. Su et al., “End-to-end deep learning model for underground utilities localization using GPR,” *Autom. Construction*, vol. 149, May 2023, Art. no. 104776.
- [17] C. Maas and J. Schmalzl, “Using pattern recognition to automatically localize reflection hyperbolas in data from ground penetrating radar,” *Comput. Geosci.*, vol. 58, pp. 116–125, Aug. 2013.
- [18] A. Dell’Acqua, A. Sarti, S. Tubaro, and L. Zanzi, “Detection of linear objects in GPR data,” *Signal Process.*, vol. 84, no. 4, pp. 785–799, Apr. 2004.
- [19] P. M. Shearer, *Introduction to Seismology*, 2nd ed., Cambridge, U.K.: Cambridge Univ. Press, 2009.
- [20] J. Zhao, S. Li, X. Zhao, and J. Feng, “A comprehensive horizon-picking method on subbottom profiles by combining envelope, phase attributes, and texture analysis,” *Earth Space Sci.*, vol. 7, no. 3, Mar. 2020, Art. no. e2019EA000680.
- [21] I. Bondár, “Seismic horizon detection using image processing algorithms,” *Geophys. Prospecting*, vol. 40, no. 7, pp. 785–800, Oct. 1992.
- [22] B. Ursin and Y. Zheng, “Identification of seismic reflections using singular value decomposition,” *Geophys. Prospect.*, vol. 33, no. 6, pp. 773–799, 1985.
- [23] N. Otsu, “A threshold selection method from gray-level histograms,” *IEEE Trans. Syst., Man, Cybern.*, vol. SMC-9, no. 1, pp. 62–66, Jan. 1979.
- [24] D. Bradley and G. Roth, “Adaptive thresholding using the integral image,” *J. Graph. Tools*, vol. 12, no. 2, pp. 13–21, Jan. 2007.

- [25] P. L. Rosin, "Unimodal thresholding," *Pattern Recognit.*, vol. 34, no. 11, pp. 2083–2096, Nov. 2001.
- [26] S. Yegireddi and N. Thomas, "Segmentation and classification of shallow subbottom acoustic data, using image processing and neural networks," *Mar. Geophys. Res.*, vol. 35, no. 2, pp. 149–156, Jun. 2014.
- [27] P. Soille, *Morphological Image Analysis: Principles and Applications*, 2nd ed., Berlin, Germany: Springer, 2002.
- [28] R. C. Gonzales and P. Wintz, *Digital Image Processing*, 4th ed., London, U.K.: Pearson, 2017.
- [29] K. Madsen, H. B. Nielsen, and O. Tingleff, *Methods for Non-Linear Least Squares Problems*, 2nd ed., Copenhagen, Denmark: DTU, 2004.
- [30] J. Pujol, "The solution of nonlinear inverse problems and the Levenberg–Marquardt method," *Geophysics*, vol. 72, no. 4, pp. 1–16, Jul. 2007.
- [31] J. V. Gardner, "The West Mariana Ridge, western Pacific Ocean: Geomorphology and processes from new multibeam data," *Geological Soc. Amer. Bull.*, vol. 122, nos. 9–10, pp. 1378–1388, Sep. 2010.
- [32] R. J. Stern, M. J. Fouch, and S. L. Klemperer, "An overview of the Izu–Bonin–Mariana subduction factory," *Geophys. Monograph Ser.*, vol. 138, pp. 175–222, 2003.
- [33] A. J. Oakley, B. Taylor, G. F. Moore, and A. Goodliffe, "Sedimentary, volcanic, and tectonic processes of the central Mariana arc: Mariana trough back-arc basin formation and the West Mariana Ridge," *Geochem., Geophys., Geosyst.*, vol. 10, no. 8, pp. 1–29, Aug. 2009.
- [34] Y. Jin, H. Wang, T. Chugh, D. Guo, and K. Miettinen, "Data-driven evolutionary optimization: An overview and case studies," *IEEE Trans. Evol. Comput.*, vol. 23, no. 3, pp. 442–458, Jun. 2019.
- [35] V. Curic, C. L. Luengo Hendriks, and G. Borgefors, "Salience adaptive structuring elements," *IEEE J. Sel. Topics Signal Process.*, vol. 6, no. 7, pp. 809–819, Nov. 2012.



Pengcheng Chen (Graduate Student Member, IEEE) received the B.S. degree in electronic information science and technology and the M.E. degree in software engineering from Southwest Petroleum University, Chengdu, China, in 2015 and 2020, respectively. He is currently pursuing the Ph.D. degree in geophysics with the School of Earth Science and Engineering, Sun Yat-sen University, Guangzhou, China.

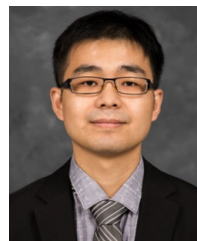
He worked as a Research Associate with the School of Resources and Environment, University of Electronic Science and Technology of China, Chengdu, in 2021. His research interests include high-performance computing, acoustic signal analysis, and image processing for geophysics.



Shaoping Lu received the B.S. degree in physics from the University of Science and Technology of China (USTC), Hefei, China, in 2004, and the Ph.D. degree in physics from The University of Texas at Austin (UT-Austin), Austin, TX, USA, in 2010.

He was a Research Geophysicist and a Senior Research Geophysicist with Petroleum Geo-Services, Inc. (PGS), Houston, TX, USA, from 2010 to 2018. He is currently a Professor with the School of Earth Science and Engineering, Sun Yat-sen University (SYSU), Guangzhou, China. His research interests include seismic data processing and imaging for exploration geophysics.

Sun Yat-sen University (SYSU), Guangzhou, China. His research interests include seismic data processing and imaging for exploration geophysics.



Chen Cai received the B.S. and M.S. degrees in geophysics from Peking University, Beijing, China, in 2009 and 2012, respectively, and the Ph.D. degree in geophysics from Washington University in St. Louis, St. Louis, MO, USA, in 2018.

He worked as a Post-Doctoral Researcher with Washington University in St. Louis, and Stony Brook University, Stony Brook, NY, USA, in 2019. He is currently an Associate Professor with the School of Earth Science and Engineering, Sun Yat-sen University, Guangzhou, China. His main research interests include passive seismic tomography of oceanic lithosphere, especially at active plate boundaries.